# $CO_2$ Electroreduction on Copper-Cobalt Nanoparticles: Size and Composition Effect

M. Bernal[1], A. Bagger[2], F. Scholten[1] I. Sinev[1], A. Bergmann[4], M. Ahmadi[1,3], J. Rossmeisl[3], B. Roldan Cuenya[1,3,4]

[1]Department of Physics, Ruhr-University Bochum, 44780 Bochum, Germany

[2]Department of Chemistry, University of Copenhagen, Universitetsparken 5, Copenhagen, Denmark

[3]Department of Physics, University of Central Florida, 32816 Orlando, USA

[4]Department of Interface Science, Fritz Haber Institute of the Max Planck Society, 14195 Berlin, Germany

*Corresponding author. Tel: +49 30 8413 4123. E-mail: roldan@fhi-berlin.mpg.de

Keywords: CO2 electroreduction, electrochemistry, nanoparticle, Copper, Surface segregation, Operando spectroscopy.

## Abstract

Understanding the changes that a catalyst may experience on its surface during a reaction is crucial in order to stablish structure/composition-reactivity correlations. Here, we report on bimetallic size-selected $Cu_{100-x}Co_x$ nanoparticle (NP) catalysts for $CO_2$ electroreduction reaction ($CO_2$RR) and we identify the optimum Cu/Co ratio and NP size leading to improved activity and selectivity. *Operando* X-ray absorption spectroscopy (XAS) and *quasi in situ* X-ray photoelectron spectroscopy (XPS) provided insight into the morphological, structural, and chemical transformations underwent by the CuCo NPs during $CO_2$RR. We illustrate that the as-prepared state of the bimetallic NPs is drastically different from the structure and surface composition of the working catalyst. Under electrochemical conditions, a reduction of both initially oxidized metallic species was observed, accompanied by Cu surface segregation. Density functional theory (DFT) results from a $Cu_3X$ model were used to describe the surface segregation. In order to extract mechanistic understanding, the activity of the experimental Cu and CuCo NPs towards $CO_2$RR was described via DFT in terms of the interaction of Cu facets under expansion and compression with key reaction intermediates, in particular CO* and COOH*.

## 1. Introduction

Copper is the most interesting and broadly studied material for the electrochemical conversion of $CO_2$ ($CO_2RR$) due to its ability to transform $CO_2$ into a diverse range of products including CO, HCOOH, $CH_4$, and also more complex C2-C3 products such as hydrocarbons and alcohols.[1–4] The unique reactivity of Cu has attracted attention to incorporate $CO_2RR$ into a closed carbon cycle based on the storage of energy in the chemical bonds of substances with high energy density (alcohols and hydrocarbons).[5] Such cycle could be powered by the surplus of energy of renewable sources, mitigating thus the emissions of $CO_2$.[6]

The electrochemical conversion of $CO_2$ on Cu electrodes faces many challenges that are the focus of extensive research.[7–11] High overpotential, competition with $H_2$ evolution, low stability, low energy efficiency and low selectivity towards a particular product are among the parameters that have to be addressed.[12,13] An attractive approach to enhance the performance of Cu electrodes is to produce bimetallic systems based on Cu. Creating a mixture of Cu with a secondary metal will affect the interaction of reactants, intermediates and products at the surface of the catalyst, enhancing or suppressing certain catalytic processes.[14,15] Furthermore, in a bimetallic system, the distribution of products is related to the surface and near-surface catalyst composition. Controlling the structure and composition of the bimetallic system constitutes a strategy to tune the activity. For $CO_2RR$, particular metal ratios in Cu-based systems have been shown to display enhanced selectivity. Carbon monoxide production is favored on metal mixtures such as Cu-Ag, Cu-Sn and Cu-In. Formate production is enhanced on Cu-Pb, Sn-Ag, Sn-Pd, and Pd-Pt materials. The production of $C_2$ products has been reported on Cu-based alloys with Ag, Zn, Pd and Pt, as well as on non-Cu based materials such as Ag-Zn and Ni-Ga, but with low yields. [16–33]

When the $CO_2RR$ catalysts are nanoparticles (NPs), other parameters affecting the activity and selectivity are the NP structure, size,[34] and shape[35–39]. The presence of undercoordinated sites can increase the activity of NPs and for a surface-sensitive reaction such as $CO_2RR$, the change in the number of undercoordinated sites may affect the product distribution.[40,41] In addition, the structure and surface composition of a bimetallic NP may differ from that of the bulk, and the exposure of the catalyst to certain environments, treatments, or reaction conditions can lead to drastic modifications which might also evolve in the course of the reaction.[42–45]

In this work, we investigate the effect of the NP size and composition of CuCo catalysts on their activity and selectivity for $CO_2$RR. The studies are conducted on well-defined NP systems, micellar NPs with narrow particle size distributions and controlled chemical composition.[46,47] Our work describes the optimum Cu/Co ratio and NP size required to enhance the $CO_2$RR. We used *quasi in situ* X-ray photoelectron spectroscopy (XPS) and *operando* X-ray absorption spectroscopy (XAS) to follow the evolution of the CuCo surface *in situ* and the local atomic structure under reaction conditions. We observed that, under electrochemical conditions, the CuCo NPs were reduced and Cu segregated to the surface. The activity of the CuCo NPs towards $CO_2$RR was described by DFT calculations[48] in terms of the interaction of the surface with key intermediates, in particular CO* and COOH*.

## 2. Experimental

### 2.1 Sample preparation

Size-controlled bimetallic CuCo NPs as well as monometallic Cu and Co reference samples were synthesized by inverse micellar encapsulation. Monodisperse micellar solutions were prepared by dissolving Poly(styrene-b-2-vinylpyridine) diblock copolymers (Polymer Source, Inc.) with different molecular weights in toluene, Table 1. Subsequently, $CuCl_2$ and $CoCl_2$ (Sigma Aldrich) salts were incorporated into the micellar solutions and stirred for two days. The composition of the NPs was then controlled by varying the metal loading of both components and the NP size by varying the size of the polymer head or the total metal loading inside a given pre-formed micellar cage. Eighteen different NP systems were prepared. A set of substrates were covered with a monolayer of NPs. Flat $SiO_2$/Si(111) wafers were used for morphological sample characterization, glassy carbon for electrochemical experiments, and carbon foil supports (Mateck) for synchrotron measurements (only the front side was covered with NPs). The NPs were then supported on the different substrates via dip-coating with an average speed of 1 cm $min^{-1}$. Polymer removal was achieved via a 20 min $O_2$ plasma etching treatment (20 W, 400 mTorr). Dip-coating and plasma etching processes were repeated consecutively five times to increase the NP coverage on the carbon surfaces.

### 2.2 Structural and chemical characterization

Nanoparticle size and geometrical surface area were determined by atomic force microscopy (AFM) using a Bruker MultiMode 8 microscope. AFM images of NPs on

$SiO_2$ acquired in tapping-mode were used to obtain the average height ($h_p$) and density of the NPs. Assuming spherical NPs, the particle height is used as representative size parameter, Table 1. The geometrical surface area of electrodes was estimated by calculating the surface area of a single particle of spherical shape and considering the NP density extracted from AFM images.

*Ex situ* X-ray photoelectron spectroscopy (XPS) measurements were conducted in an ultra-high vacuum (UHV) system with a monochromatic Al Kα source (hν = 1486.5 eV) operated at 300W and 14.5 kV, and with a Phoibos 150 analyzer (SPECS GmbH). Survey and high resolution XPS spectra from the C 1s, O 1s, Cu 2p and Co 2p core level regions were measured on NP samples supported on $SiO_2$/Si. The $Si^0$ peak at 99.3 eV was used as reference to align the data.

*Quasi in situ* XPS measurements were carried out in an UHV system with a non-monochromatic Al source (hν = 1486.5 eV) and a hemispherical Phoibos 100 analyzer (SPECS GmbH). Electrochemical treatment of the samples supported on glassy carbon was performed in an electrochemical (EC) cell connected to the XPS system using an Autolab pontentiostat (PGSTAT 302N). The sample transfer to the XPS chamber was done under vacuum. Once the XPS spectrum was recorded, the sample was transferred back into the EC cell and the process was repeated after different $CO_2$RR times ranging from 1 min to 60 min. The current XPS measurements were not conducted under operando electrochemical reaction conditions, but after the electrochemical treatment. The electrochemical reaction chamber is however directly attached to the XPS-UHV system, allowing sample transfer without air exposure.

The CuCo NPs were also studied under $CO_2$RR *operando* conditions at -1.1 V vs. RHE by X-ray absorption fine-structure spectroscopy (XAFS) at the Cu-K (8979 eV) and Co-K (7709 eV) absorption edges. The measurements were conducted at the undulator beamline P65 of Petra III storage ring operating in top-up mode at 6 GeV. A custom made *operando* cell was used, in which carbon foil electrodes coated with NPs were mounted as an X-ray window. The back side of the electrode was sealed with Kapton tape and the front side (WE) was exposed to the electrolyte constantly purged with $CO_2$. The measurements were executed in fluorescence mode using a 7-pixel high purity germanium detector (HPGe, Canberra). Multiple identical spectra were recorded for each sample (20 min recording time) and then averaged to improve the signal to noise ratio. Initial reduction of the XAFS data was done with the Athena program. Coordination numbers (CN), interatomic distances (r) and disorder parameters ($\sigma^2$) of the CuCo NPs were obtained by analyzing the extended X-ray absorption fine-structure (EXAFS) data with Artemis using a FEFF6 code.[49,50]

### 2.3 Electrochemical measurements

$CO_2$RR experiments were carried out at constant potential in a custom-made H-type electrochemical cell. The compartments of the cell were separated by a Selemion ion exchange membrane. A leak free Ag/AgCl (Innovative Instruments, Inc.) electrode and a platinum mesh (MaTeck 3600 $cm^{-2}$) were used as reference electrode (RE) and counter electrode (CE) respectively. The working electrode (WE) consisted of a glassy carbon plate covered with NPs (4.6 $cm^2$ exposed area). Every experiment was conducted on an identically-synthesized fresh sample. The reaction was conducted in 40 mL of 0.1 M $KHCO_3$ (Sigma-Aldrich, 99.7%) purged with a constant flow of $CO_2$ (20 mL/min). The applied potential, -1.1 V vs RHE, was controlled with an Autolab potentiostat (Multi Autolab/M204). The current interrupt technique was used to determine the resistance (R) used to correct the potential for *iR* drop. The same RE and CE, $CO_2$-saturated electrolyte and applied potential were used in the synchrotron and *quasi in situ* XPS experiments. The reported current densities were normalized by the geometrical surface area obtained from AFM measurements.

The analysis of the gases produced in the working electrode was done online by gas chromatography (GC, Shimadzu 2014). Hydrocarbons were separated through HayeSepQ + HayeSepR packed columns and detected in a flame ionization detector (FID). $H_2$, $N_2$ and $O_2$ were separated by a MS-13X column and analyzed by a thermal conductivity detector (TCD). CO and $CO_2$ are methanized and detected by FID. Liquid products from the reaction were accumulated in the electrolyte and detected via high-performance liquid chromatography (HPLC, Shimadzu Prominence) in a NUCLEOGEL SUGAR 810 column and analyzed in a refractive index detector (RID). The analysis of alcohols was performed with a liquid GC (Shimazu 2010 plus) that was equipped with a silica capillary capillary column and FID. The product quantification and current recorded after 1 h of $CO_2$RR were used to calculate faradaic selectivity. Background $H_2$ concentration and current produced by the glassy carbon support were subtracted from each Faradaic selectivity calculation.

## 2.4 Density Functional Theory calculations

Two approaches were used to represent the bimetallic NPs and calculate binding energies of reactants, intermediates and products: a $Cu_3X$ bimetallic model, and Cu facets with varying lattice constants.

For the $Cu_3X$ bimetallic system, first the lattice constant of each bimetallic was optimized in a 2x2x2 bulk unit cell created with ASE[51], with periodic boundaries, (7x7x7) k-points and the RPBE functional[52] as implemented in GPAW.[53] From each of the optimized bulk alloys, three (2x2x4) surface slabs were constructed in the $Cu_3X$ composition, in a Cu skin layer composition by transferring the surface X atoms to the second layer, and an X skin layer composition obtained by moving the second layer X atoms to the surface. The slab structure energies were calculated with periodic boundary conditions in the xy-plane, a grid spacing of 0.18 Å, (4x4x1) k-points, and the RPBE functional. Then, the most stable structure obtained by:

$$\Delta E_{formation} = E_{slab} - E_{Cu_3X} \text{ , slab= \{Cu}_3\text{X, Cu skin, X skin\}}$$

, where the reference made to the $Cu_3X$ composition shows if Cu or metal X will segregate to the surface.

For the Cu facets, the trends in the binding energy of the key intermediates were studied by varying the lattice constant in a Cu slab (3x3x4) model with periodic boundaries in the xy-plane, a vacuum spacing of minimum 15 Å, a grid spacing of 0.18 Å, (4x4x1) k-points and the BEEF-vdW functional.[54] Using the BEEF-vdW functional allowed us to estimate the uncertainty in our calculated binding energies when perturbing the Cu lattice constant in our previous trend scheme[48] by referring these contracted or expanded Cu(hkl) binding energy ensembles to the Cu(hkl) facet with a lattice constant of 3.69 Å. For each Cu (111), Cu (100), Cu (110) and Cu (211) facet with lattice constant 3.69 Å, the binding energies are found with respect to gas phase without plotting the uncertainty related to gas phase molecule references.

## 3. Results and discussion

AFM was used to observe the size and dispersion of the NPs, Figure 1. Additional images for the remaining systems studied and the NP height histograms are included in the supplementary information (Figs. S1 and S2) and Table 1. The AFM images show that the NPs have homogenous size ranging from 1.2 to 21 nm in the different samples investigated.

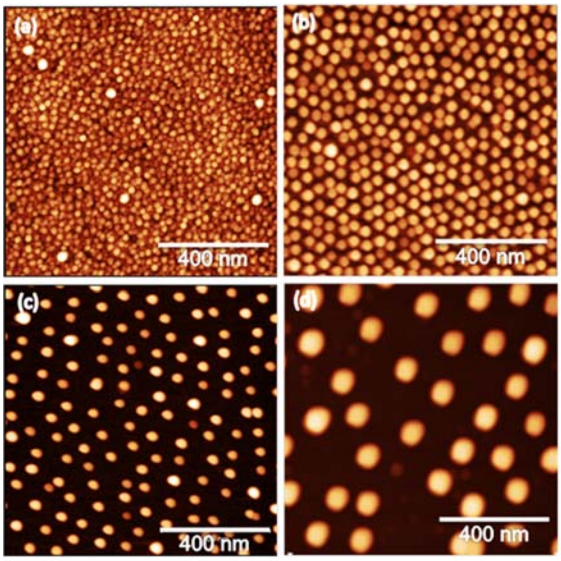

**Figure 1.** AFM images of $Cu_{50}Co_{50}$ NPs of different average sizes supported on $SiO_2$/Si (111). The average NP size is: (a) 2.7 nm (S2) (b) 5.2 nm (S3) (c) 11.6 nm (S4), (d) 20.7 nm (S5).

| **Size** | **Polymer** | **Metal Loading** | **$Cu_{50}Co_{50}$ Particle Size $h_p$ (nm)** | **$Cu_{70}Co_{30}$ Particle Size $h_p$ (nm)** | **$Cu_{90}Co_{10}$ Particle Size $h_p$ (nm)** |
|---|---|---|---|---|---|
| S1 | PS(16000)-P2VP(3500) | 0.2 | 1.2 ± 0.3 | 1.3 ± 0.5 | 1.6 ±0.6 |
| S2 | PS(91000)-P2VP(10000) | 0.3 | 2.7 ± 0.8 | 2.7 ± 0.6 | 2.9 ±0.1 |
| S3 | PS(48500)-P2VP(70000) | 0.2 | 5.2 ± 1.2 | 5.1 ± 0.6 | 5.3 ± 0.8 |
| S4 | PS(130000)-P2VP(135000) | 0.5 | 11.6 ± 1.9 | 11.4 ± 1.7 | 12.28 ± 1.7 |
| S5 | PS(130000)-P2VP(135000) | 0.5 | 20.7 ± 2.4 | 21.13 ± 3.7 | 21.37 ± 3.0 |

**Table 1.** Parameters used for the synthesis of CuCo NPs by micelle encapsulation together with the AFM NP heights. The metal loading is the ratio of the molecular weight of the metal salt versus that of the polymer head (P2VP).

The surface composition of the CuCo NP pre-catalysts was determined by XPS. We consider as pre-catalyst the NPs deposited on a substrate after polymer removal with $O_2$ plasma but before $CO_2$RR, because the NPs will be activated to their catalytic state when electrochemical conditions are applied. Figure 2 shows XP spectra of the Cu 2p and Co 2p core-level regions of $Cu_XCo_{100-X}$ NPs (X = 30, 50, 70, 90) with a size of ~5.2 nm. An XPS survey scan is presented in Figure S3. In all spectra, the Cu and Co 2p core level regions exhibit characteristics typical of oxides, including shake-up satellites features found for the 2+ oxidation state of the first row transition metals.[55,56] The intensity of the respective XPS peaks vary according to the nominal metal content, although all samples showed copper surface enrichment as can be seen in Table S1.

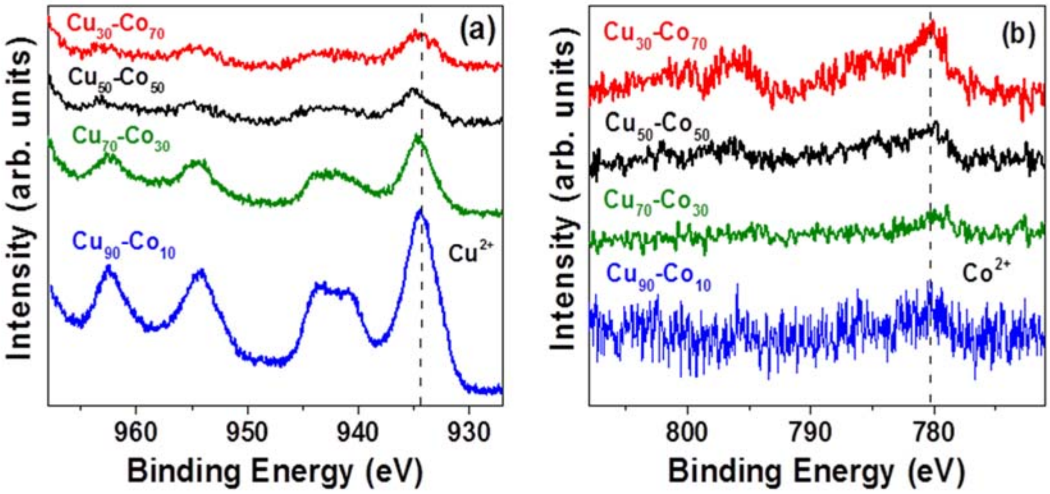

**Figure 2.** *Ex situ* high resolution XPS spectra of the (a) Cu-2p and (b) Co-2p core level regions of $Cu_{90}Co_{10}$, $Cu_{70}Co_{30}$, $Cu_{50}Co_{50}$ and $Cu_{30}Co_{70}$ NPs with average size of ≈5.2 nm supported on $SiO_2$/Si (111).

The effect that the metal composition has on the activity of $CO_2$RR on CuCo NPs is shown in Figure 3. The reaction was carried out on NPs of the same size (S3, ≈ 5.2 nm) but with varying composition ranging from pure Co to pure Cu. The current density of $Cu_XCo_{100-X}$ NPs decreased as Cu was incorporated into the NPs, however, a content of 90% Cu in the pre-catalyst was found to lead to the highest activity, Figure 3a. The analysis of the partial current density (Figure S4a) revealed that HER is the main reaction on $Cu_XCo_{100-X}$ and the only one on pure Co NPs. The decrease in current density is due to the suppression of HER by the competition with $CO_2$RR. Increasing the Cu content in the NPs favors $CO_2$RR. The highest $CO_2$ conversion was observed at a Cu content of 90%.

Faradaic selectivity of $CO_2RR$ on CuCo NPs calculated from the current density and product concentration (normalized to 100 %) is presented as a function of Cu content in Figure 3b. On Co NPs the only product is $H_2$, with only traces of CO and HCOOH being detected.[2,3] As the Cu content in the NPs increases, HCOOH and CO were the main products detected, in that order of abundance. The activity towards $CO_2RR$ versus hydrogen evolution reaction (HER) improved with increasing Cu content in the NPs. The highest selectivity for HCOOH and CO was observed for a Cu content of 90% Cu, exceeding the performance of the pure Cu NPs. However, $H_2$ was still the main product, although the $Cu_{90}Co_{10}$ NPs produced the lowest amount of $H_2$,[57] corroborating that small amounts of Co can have a beneficial effect in the electrochemical conversion of $CO_2$ over Cu-based materials.[24] Nevertheless, despite the high content of Cu, CuCo NPs produced only traces of $CH_4$ and no other hydrocarbon or alcohol was detected.

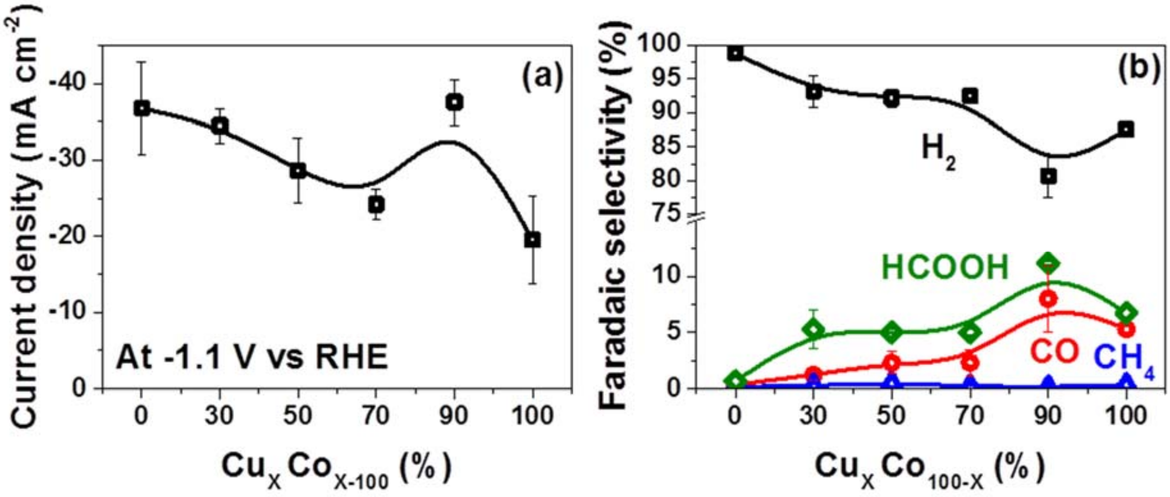

**Figure 3.** (a) Current density and (b) Faradaic selectivity of Cu, Co and $Cu_xCo_{100-x}$ NPs after 1 hour of $CO_2RR$ at E= -1.1 V vs RHE as a function of the Cu content at constant NP size (S3 ≈5.2 nm).

Based on the activity results of the composition study, we decided to explore the effect that particle size has on the $CO_2RR$ on CuCo NPs of different Cu content. Nanoparticles of five different particle sizes were produced for $Cu_XCo_{X-100}$ systems with X=50, 70, and 90, (Table 1). The total current density of CuCo NPs as a function of the particle size at -1.1 V vs. RHE, Figure 4a, showed that the smallest NPs were the most active. As the particle size increased, the activity of the NPs decreased, due to a lower number of undercoordinated sites.[34,40,41] The intense evolution of $H_2$ for NPs during

$CO_2RR$ has been attributed to the presence of undercoordinated sites. Small NPs having a larger number of undercoordinated sites are more active towards $H_2$ evolution.[40]

In Figure 4 (b, c, d) the effect of the NP size on the selectivity of CuCo NPs of different nominal metal composition (Cu = 50 %, 70 %, 90 %) is shown. In the three cases it can be seen that $H_2$ production decreases as the NP size increases, in parallel with an increase in the selectivity for $CO_2RR$ products. Moreover, for the smallest particles (S1), the increase in Cu content lead to an improvement of the selectivity towards $CO_2RR$ vs HER. Nevertheless, in all cases, $H_2$ was the most abundant product. On small NPs (S1 and S2) the production of CO and HCOOH was dependent on the Cu content. The enrichment with Cu raised the CO production, while the enrichment with cobalt benefited HCOOH production. The product distribution observed in Figure 3b for the 5.2 nm NPs remains, being HCOOH the main product of $CO_2$ reduction followed by CO for all different compositions. For $Cu_{50}Co_{50}$ NPs the increase in $CO_2RR$ vs HER selectivity is not very significant, contrary to the Cu-enriched particles which showed a major enhancement in the production of HCOOH and CO. The partial current densities presented a similar behavior (Figure S4). In the case of $Cu_{90}Co_{10}$ NPs, the increase in particle size did not favor the production of hydrocarbons, indicating that the intermediates necessary for the production of hydrocarbons or alcohols were not stabilized on the surface of the NPs.[48,58] Such hypothesis lead to investigate with DFT the influence of the stability of key intermediates at the catalysts surface on their selectivity towards CO2RR, as it discussed in the following sections.

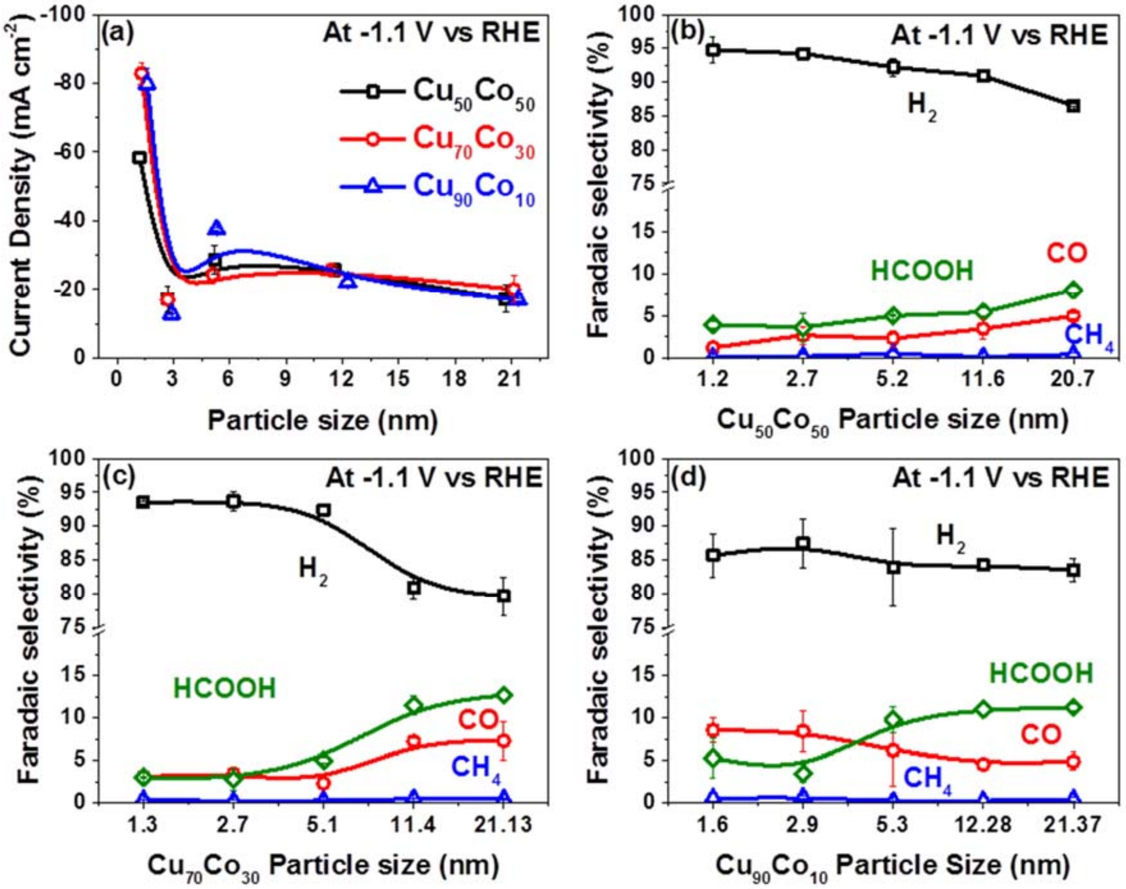

**Figure 4.** (a) Current density as a function of particle size of Cu$_x$Co$_{100-x}$ NPs. Faradaic selectivity as a function of NP size for the following bimetallic compositions: (b) Cu$_{50}$Co$_{50}$ (c) Cu$_{70}$Co$_{30}$ (d) Cu$_{90}$Co$_{10}$. The data were recorded after 1 hour of CO$_2$RR at E= -1.1 V vs RHE.

Changes on the surface chemical state and composition of the CuCo NPs due to the exposure to reaction conditions were examined by *quasi in situ XPS* using an electrochemical cell directly attached to the UHV setup. This allows us to transfer the samples in UHV after electrochemical testing preventing re-oxidation in air. The spectra were obtained in the as-prepared state and after various CO$_2$RR reaction times (1, 2.5 and 60 min) in order to monitor the evolution of the composition and chemical state of the NP surface and also NP sintering indirectly through signal attenuation. Figure 5 displays the Co and Cu 2p XPS spectra of Cu$_{50}$Co$_{50}$ NPs with sizes of (a) 2.7 (S2) and (b) 11.6 nm (S4). Analogous data for NPs of 5.2 nm and 20.7 nm nominal size are shown in Figure S5. All spectra are aligned to the carbon peak (E$_{bin}$ = 284.8 eV) since glassy carbon was the employed substrate. The XPS data reveal that before applying a potential of -1.1V vs RHE both metals are oxidized (Cu$^{2+}$ and Co$^{2+}$) and present within the particle surface. Upon applying the potential for only 1 minute the copper is reduced in the case of both particle sizes. The Cu 2p core level spectra of $Cu^+$ and metallic Cu do not differ significantly.[55] However, for our highly dispersed NPs a discrimination between $Cu^+$ and metallic Cu using the Cu LMM Auger spectra was not possible due to the low metal loading.

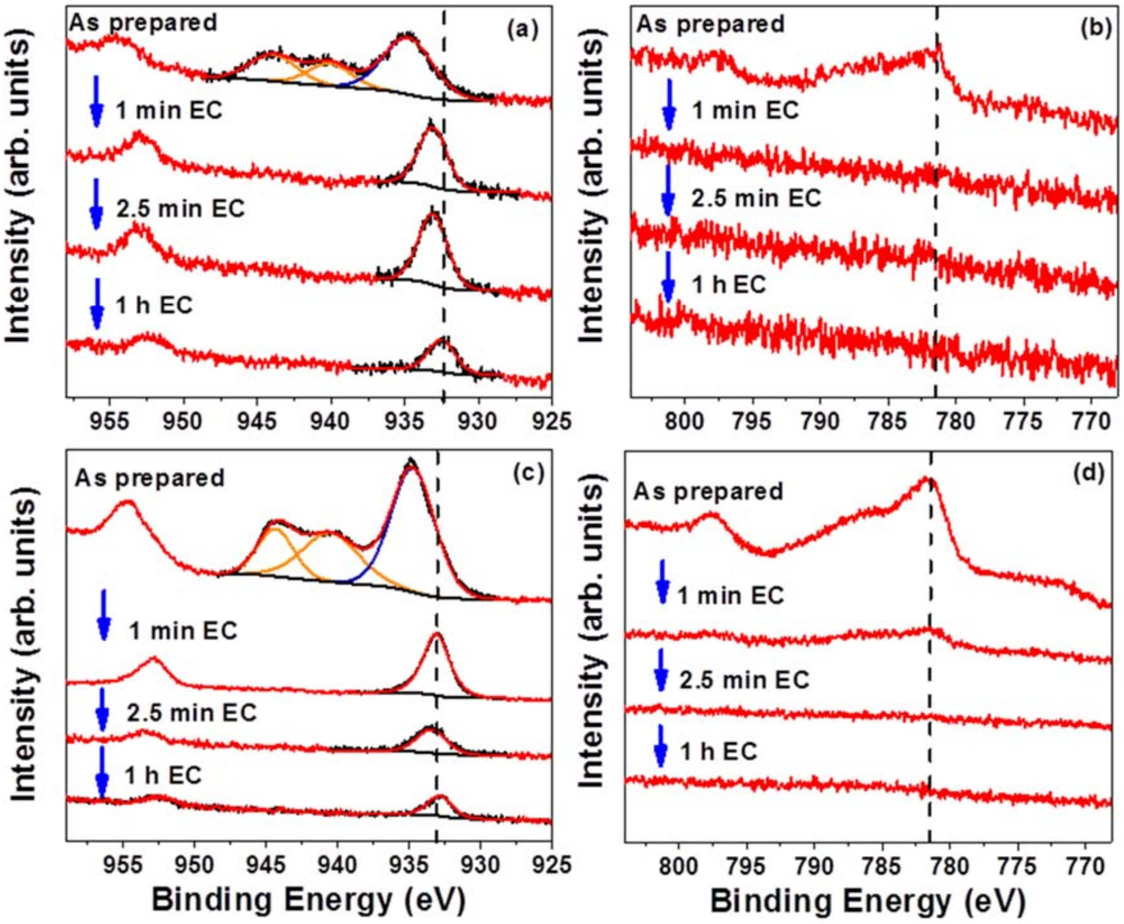

**Figure 5.** *Quasi in situ* XPS spectra of the Cu-2p (a,c) and Co-2p (b,d) core level regions of $Cu_{50}Co_{50}$ NPs supported on glassy carbon. The NPs with average size of 2.7 nm (S2) are shown in (a,b) and those 11.6 nm (S5) in size are displayed in (c.d). The spectra were acquired after various $CO_2$RR times at -1.1V vs RHE.

A significant decrease in the intensity of the Co peaks was observed with increasing reaction time, while the Cu peaks changed less drastically. In the case of the 11.6 nm NPs, a possible explanation for the progressive loss of the Co signal taking into account the electron inelastic mean free path (IMFP) of 2.1 nm[59] is that the particles form a core-shell structure where Co accumulates in the core. However, in the case of the 2.7 nm NPs a similar loss of Co signal can be seen with XPS, even though in this case the entire NP is probed. Thus, either cobalt leaches into the solution and is lost from the NPs, or the NPs grow in size significantly during $CO_2$RR hiding a possibly Co-enriched NP core from XPS analysis, Figure S6.[59] As it can be seen in Figure 5, the Cu signal also decreased with time during $CO_2RR$ although it never disappeared. Thus, Cu can still be predominantly found on the NP surface under reaction conditions, but this also suggests that the NPs have possibly sintered. The dashed vertical lines in Figure 5 (a, c) mark the binding energy that is expected for bulk metallic Cu ($E_{bin}$ = 932.67 eV). Initially, the Cu-2p peaks are shifted to a higher BE due to the oxidized state of the Cu atoms but were found to move towards the lower binding energy with increasing reaction time after 1 min. This change is clearer for the 2.7 nm sample, for which a positive BE shift is still observed within the first minutes of the reaction, and only disappears after 1 h. This shift is assigned to initial and final state effects typically observed for NPs smaller than about 5 nm. The same trend is not seen for the 11.6 nm sample, for which the bulk BE of Cu is already achieved during the first minute of the reaction after the initial reduction of the $Cu^{2+}$ species.

We have ruled out the possible loss of cobalt (dissolution from the NP surface into the electrolyte) by conducting AFM measurements of pure Co NPs supported on highly-oriented pyrolytic graphite (HOPG) before (open circuit potential - OCP when the samples are first introduced into the electrolyte) and after $CO_2RR$ at -1.1 V versus RHE, Fig. S7. Figure S7 demonstrates lack of drastic morphological changes for the pure Co NPs, including no decrease in particle height (average 5.8 nm) or disappearance of the NPs under OCP in 0.1 M $KHCO_3$ during the short times where the drastic changes in the Co XPS signals are seen. The same applies to the samples treated at -1.1 V versus RHE. These images were conducted in parallel to *quasi in situ* XPS measurements on identically prepared $Cu_{50}Co_{50}$ NPs with 20.7 nm size (S5). When $Cu_{50}Co_{50}$ (20.7 nm) NPs were measured via XPS after 1 min of electrolyte immersion under OCP. No decrease of the Co 2p signal was observed, Fig. S8, this confirms that the disappearance of the Co signal is not due to the immediate leaching of cobalt into the electrolyte.

Summarizing, our *quasi in situ* XPS data reveal that Cu segregates to the NP surface and that NP sintering (no loss of Co) takes place already upon electrolyte exposure at OCP but more significantly under reaction conditions for all samples, leading to the partial/total loss of the XPS Co signal. The confirmation by XPS that the surface of the CuCo NPs is rich in copper is in agreement with the activity and selectivity of CuCo NPs towards $CO_2RR$ presented in Figures 3 and 4. $CO_2RR$ took place over Cu surfaces, while over Co surfaces only $H_2$ was produced. To corroborate these findings, a bulk-sensitive technique, XAFS was used in order to be able to map the composition of the entire NPs.

Insight into the local coordination and chemical state of CuCo NPs under $CO_2$RR was obtained via *operando* XAFS measurements. X-ray absorption near-edge structure (XANES) spectra of $Cu_{50}Co_{50}$ NPs of 11.6 nm (S4) were acquired at the Cu K-edge and Co K-edge of the as prepared samples and those under $CO_2$RR conditions (-1.1 V vs. RHE), Figure 6 (a,c). Subsequently, the EXAFS data were analyzed to identify the local atomic structure around the Cu and Co atoms, Figure 6 (b, d). It was observed that the as prepared NPs are completely oxidized and got reduced towards the metallic state under reaction conditions. It should be noted however that the first XAFS scan was obtained after 20 min of reaction, i.e., after the main changes reported in the XPS spectra (Figure 5) already happened on the NP surface. Moreover, multiple scans needed to be recorded and averaged to improve the signal to noise ratio.

The Cu and Co K-edge XANES spectra of the as prepared NPs (Figure 6a and 6c) exhibit oxide-typical features at ~8998 eV and at ~7725 eV, respectively. Comparing these spectra with the spectra of the oxide references (see also Figure S9) shows that the Co and Cu atoms are predominantly present in oxidation state +2, which agrees well with XPS results discussed above. Fitting of the EXAFS spectra recorded at the Cu K-edge revealed that Cu ions are in first approximation four-fold O-coordinated with a mean Cu-O distance of 1.95±0.02 Å. This distance agrees well with a $Cu^{2+}$-O as present in a Tenorite-like CuO.[60] The second coordination shell of the Cu ions can be hardly seen in the Fourier Transform (FT)-EXAFS and no analysis could be performed on Cu-M distances.

The quality of the Co EXAFS data is significantly worse, and therefore, we were not able to extract reliable coordination numbers and distances from the EXAFS fits. However, the strong peak in the FT-EXAFS at reduced distances of ~1.5 Å and ~2.65 Å indicates the presence of a significant fraction of Co-O distances and di-μ-oxo-bridged $Co^{2+}$ ions in the as-prepared $Cu_{50}Co_{50}$ NPs.

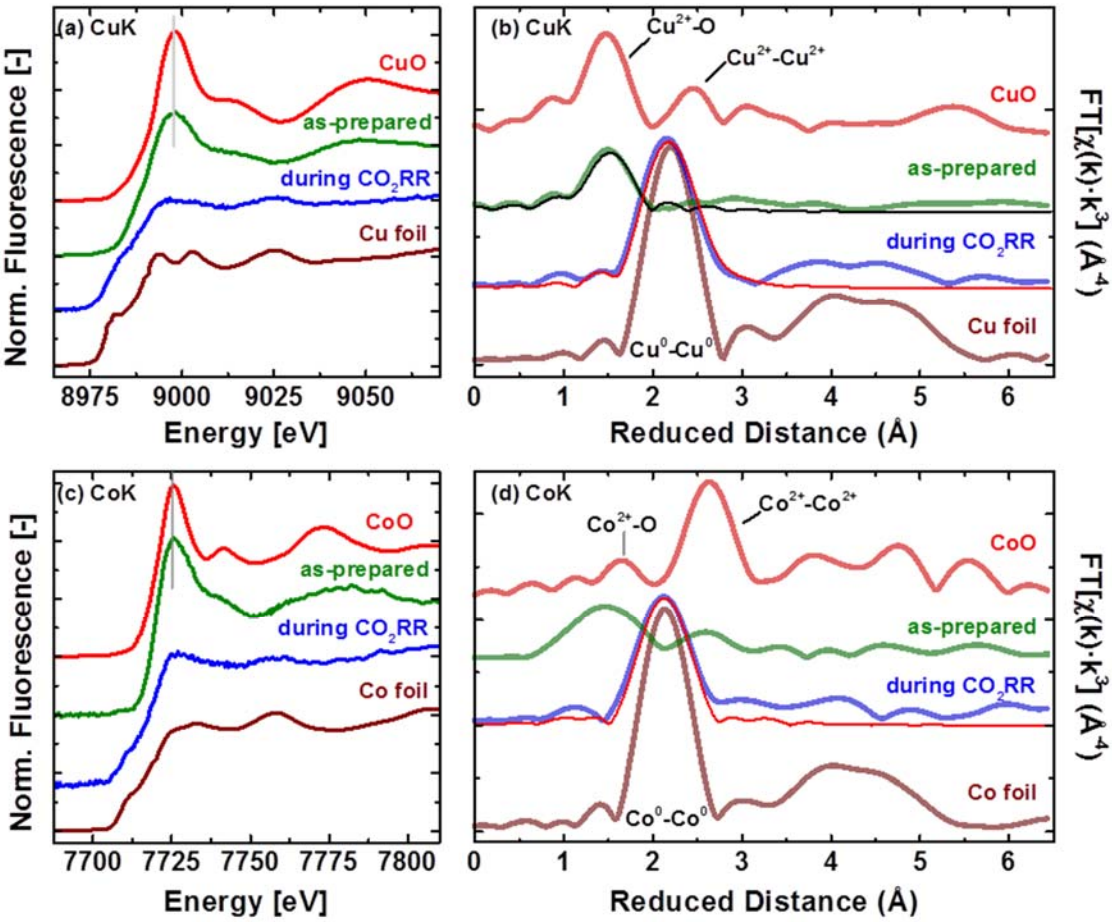

**Figure 6.** (a) Cu K-edge and (c) Co K-edge XANES and respective EXAFS data (b,d) of $Cu_{50}Co_{50}$ NPs of 11.6 nm (S4) measured as prepared in air and under *operando* $CO_2$RR at -1.1 V vs RHE in 0.1 M $KHCO_3$. The thin lines in (b,d) are the fits of the EXAFS data. Reference spectra from bulk Cu, Co foils and CuO and CoO are also shown for comparison. The features typical of oxides in the Cu and Co K-edge XANES spectra at ~8998 eV and at ~7725 eV, respectively, are marked with grey lines in (a) and (c). The peaks of the most important absorber-backscatterer distances in the FT-EXAFS of the reference materials are labelled in (b) and (d). The $Co^{2+}$-$Co^{2+}$ distance corresponds to a di-μ-oxo bridged pair of $Co^{2+}$ ions. The corresponding EXAFS spectra are shown in Figure S9.

*Operando* XANES data of $Cu_{50}Co_{50}$ NPs show that the intensity of the oxide-typical features significantly decreased under $CO_2$RR conditions. The XANES profiles follow closely the spectra of the metallic Cu and Co references. The Cu K-edge XANES spectrum of the $Cu_{50}Co_{50}$ NPs exhibits the pre edge (8981 eV) and post edge features

(8993 eV and 9002 eV) of a Cu foil. However, the features of the XANES spectra of the NPs are less pronounced than in the reference spectra which complicates the identification of remaining $Cu^+$, $Cu^{2+}$ or $Co^{2+}$ ions under reaction conditions. The weak maximum of the XANES profiles at ~8998 eV and at ~7725 eV recorded can be caused by the presence of some residual cationic Cu and Co species. The more pronounced feature at 7725 eV of the Co K-edge spectra suggests a higher degree of oxidation for the Co than for the Cu atoms. Thus, the *operando* XANES data indicate that the NPs are possibly partially oxidized during $CO_2RR$.

Analysis of the *operando* EXAFS spectra revealed that the electrochemical reduction of the metal ions under $CO_2RR$ changed the local atomic structure from a CuO-like $CuO_4$ coordination towards a metal-like first coordination shell. The best results were obtained by fitting Cu-Cu and Co-Co components, yielding distances of ~2.49 ± 0.01 Å and 2.50 ± 0.01 Å, respectively. The Cu-Cu distances are shorter than those expected for bulk-like Cu NPs (2.556 Å), whereas the Co-Co distances were similar to the bulk distance of 2.502 Å.[60] The shorter interatomic distances can be explained with a particle size effect as the metallic lattice contracts with decreasing domain size.[61–63] The coordination number of the Co-Co distances (8.0 ± 0.5) under $CO_2RR$ was only slightly larger than the one of the Cu-Cu distances (7.8 ± 0.6), indicating that despite their initial nominal large size, the NPs are non-bulk like. As the XANES spectra suggest oxide species in the NPs during $CO_2RR$, Cu-O and Co-O distances were also implemented in the EXAFS fit. The fits indicate the presence of $Co^{2+}$-O with a distance of 2.05 ± 0.02 Å and possibly traces of residual $Cu^{2+}$-O. Interestingly, the EXAFS fitting suggests also the presence of shorter Co-O or Co-C distances of 1.75 ± 0.04 Å that could be explained with the formation of cobalt carbonyl hydride species during $CO_2RR$.[64] However, we should to note that the coordination numbers for the M-O/C distances exhibit fit errors of similar size.

Thus, our *operando* XAFS analysis shows that the $Cu_{50}Co_{50}$ NPs under reaction conditions can be best described as mainly metallic NPs. The stronger contraction of the Cu-Cu distances compared to the Co-Co distances agrees well with the Cu surface segregation forming a comparably thin Cu-rich shell with a contracted lattice on a Co-rich core of the NPs. The Co-rich core might also exhibit some remaining oxide species.

| | CN | r / Å | σ / Å |
|---|---|---|---|
| **as prepared $Cu_{50}Co_{50}$** | | | |
| Cu-O | 4 ± 1 | 1.94 ± 0.02 | 0.07 ± 0.02 |
| **$Cu_{50}Co_{50}$ during $CO_2RR$** | | | |
| Cu-O | 0.3 ± 0.5 | 1.95 ± 0.2 | 0.07 ± 0.02 |
| Cu-Cu | 7.8 ± 0.6 | 2.49 ± 0.01 | 0.088 ± 0.001 |
| Co-O | 0.7 ± 0.5 | 1.75 ± 0.05 | 0.07 ± 0.02 |
| Co-O | 1.7 ± 0.9 | 2.05 ± 0.02 | 0.07 ± 0.02 |
| Co-Co | 8.0 ± 0.5 | 2.50 ± 0.01 | 0.088 ± 0.001 |

**Table 2.** EXAFS fit parameters: coordination number (CN), interatomic distance (r), disorder parameter (σ) extracted from the analysis of Cu K-edge and Co K-edge data of $Cu_{50}Co_{50}$ NPs of 11.6 nm (S4) measured *operando* during $CO_2RR$ at -1.1 V vs RHE in $KHCO_3$ (0.1M). Disorder parameter of the M-O and M-M distances were jointly-fitted.

To understand the Cu surface segregation of the CuCo NPs, a $Cu_3X$ model was created. The results from the tested Cu bimetallic systems are shown in Figure S10. $Cu_3X$ models that have a Cu skin with the lowest energy are of primarily interest for $CO_2RR$ experiments, which corresponds to $Cu_3Co$, $Cu_3Fe$ and $Cu_3Ni$ bimetallics. Hence, this model follows the previous segregation results of bimetallics [65] and clearly describes the observed Cu surface segregation in Figure 5 and Figure 6 for the CuCo NPs.

Having a Cu skin on top of a set of CuCo NPs with different Co weight % perturbs the selectivity between $CO_2RR$ and the unwanted HER as shown by the faradaic selectivity results in Figure 3b, as compared to pure Cu NPs. Combining the performance change of the CuCo NPs with the observed EXAFS contraction of the interatomic Cu-Cu distances as compared to bulk, on Table 2, motivates the investigation of the effect that lattice contraction or expansion has on the binding energy of key intermediates of $CO_2RR$ and HER on multiple Cu facets and subsequently, on the product selectivity of CuCo NPs towards $CO_2RR$.[48]

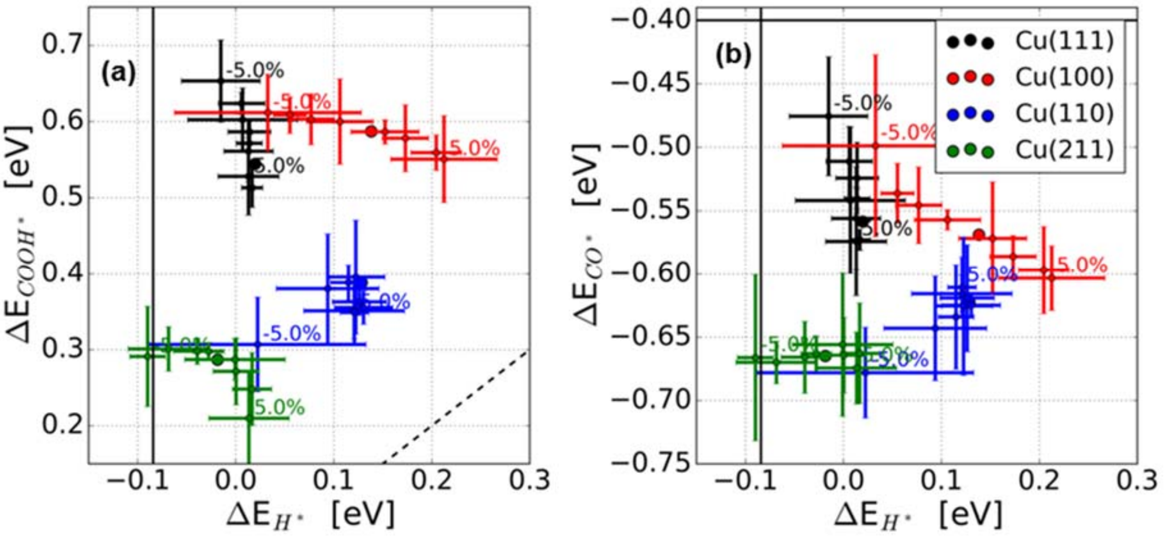

**Figure 7.** (a) Binding energy of the intermediate COOH* vs H* and (b) binding energy of CO* vs H* for Cu facets. The black vertical lines in (a) and (b) correspond to hydrogen binding $\Delta G_{1/2H2\text{-}> H*}$. In (a) the dashed lines is the diagonal of the two binding energies ($\Delta E_{H*} = \Delta E_{COOH*}$) and in (b) the vertical line correspond to carbon monoxide binding $\Delta G_{CO(g)\text{-}> CO}$. In (a) and (b) the lattice expansion and contraction ranges from -5% to 5% as written in the figures, and the error bars are given from the BEEF-vdW functional with respect to the none perturbed facet calculation, while the none perturbed facet energy is set with respect to gas phases without error bars.

The binding energy trend study of Cu(111), Cu(100), Cu(110) and Cu(211) for the most important intermediates for CO$_2$RR, COOH* vs. H* and CO* vs H* is shown in Figure 7(a, b), respectively. The vertical line corresponds to $\Delta G_{1/2H2\text{-}> H*}$ in both Figure 7a and 7b, the horizontal line of Figure 7b to $\Delta G_{CO(g)\text{ -}> CO*}$ and the dashed black line in Figure 7a to $\Delta E_{H*} = \Delta E_{COOH*}$. Without discussing reaction pathways and only observing the binding energy trends in Figure 7a, an energetically better CO$_2$RR catalyst should move towards the dashed black line. This can be obtained by utilizing that the COOH* intermediate binds ontop vs the H* intermediate binding to the hollow site,[66] and hence perturbing the lattice constant affects these intermediates differently on the facets as seen in Figure 7a and 7b. However, the improved binding energy corresponds to an expansion and not a contraction as observed in the Cu-Cu interatomic distance of the CuCo NP alloys. Further, to obtain products beyond CO, our descriptor plot is shown in Figure 7b. Here, the Cu catalyst requirement is to bind CO* stronger, which is similarly observed by an expansion and not a contraction. Hence, we understand from this lattice expansion and contraction study of the Cu facets why the CuCo NPs have a higher selectivity towards $H_2$ than towards CO$_2$RR related products as compared to pure Cu, by having a less strong COOH* binding as compared to H*. Further, the CuCo NPs produce almost no product beyond CO* which is shown by the weaker binding of CO* on the Cu facets due to the Cu-Cu contraction.

From the combined studies on CuCo NPs it is clear that their activity towards $CO_2RR$ is dominated by the chemical and morphological transformations they suffered under electrochemical conditions. Varying the NP composition showed that small amounts of Co can improve the activity of CuCo NPs towards $CO_2RR$ by the creation of highly active sites due to Cu surface segregation. The study of the effect of particle size corroborated that as particles grow in size, $CO_2RR$ is favored (versus HER) due to the decrease in the content of undercoordinated sites and presumably a lower degree of lattice contraction. *Quasi in situ* XPS and *operando* XAFS studies revealed that the oxidized CuCo NP pre-catalysts were basically reduced to metallic state. This reduction occurred in a short time and induced surface segregation of Cu as indicated by XPS. The results from the *operando* XAFS study are in agreement with the Cu surface segregation and determined that the resulting structures present low coordination numbers and a contraction of the M-M interatomic distances. DFT calculations of $Cu_3X$ models ratified the stability of CuCo NPs with an enriched Cu surface. The investigation of the lattice contraction or expansion of different Cu facets of CuCo NPs indicated that HER is favored over $CO_2RR$ due to the contraction of Cu-Cu interatomic distance estimated by XAFS. The low production of hydrocarbons and absence of alcohol products observed for our catalysts was assigned to the lower stability of the reaction intermediates over small and highly defective nanoparticles[40,67] where the Cu-Cu interatomic distances are also contracted. According to the present DFT calculations, such contraction leads to a weaker CO* and COOH* binding that hinders the formation of products beyond CO*.

## 4. Conclusions

In summary, we have explored the effect that metal composition and particle size have on the activity of $CO_2RR$ over well-defined CuCo NPs synthesized by inverse micellar encapsulation. The characterization of the as prepared samples revealed the narrow size distribution of the NPs and that initially both metals in the as prepared NPs were oxidized. The faradaic efficiency and partial current density of $CO_2RR$ experiments showed that small amounts of Co benefit the activity of CuCo NPs, while an increase in particle size favors $CO_2RR$ over HER. Under reaction conditions the NPs underwent Cu surface segregation and possibly sintering as it was observed by *in situ* and *operando* spectroscopic methods. The stability of such Cu-rich skin/Co-rich core systems was corroborated by theoretical calculations. The performance of CuCo NPs towards $CO_2$RR was explained by the contraction of the Cu-Cu interatomic distance that weakens the binding energy between the surface and key intermediates COOH*, CO* and H*. In this work we demonstrated the relevance of *in situ* and *operando* techniques to characterize the evolution of a catalyst while at work. The information acquired under reaction conditions is crucial to determine the actual nature of the catalytically active surface and to obtain parameters that may be helpful to gain mechanistic understanding of the studied reaction. Finally, our study revealed that more effective $CO_2$RR bimetallic nanoscale catalysts can be achieved if under reaction conditions one is not only able to stabilize Cu at the NP surface, as it is the case here, but if additionally the metal in the core of the NP is able to induce a significant expansion in the Cu-Cu lattice.

## Acknowledgments

We thank Dr. Hyo Sang Jeon for helpful discussions. This work was supported by IMPRS-SURMAT (MB), the German Federal Ministry of Education and Research (Bundesministerium für Bildung und Forschung, BMBF) under grant #03SF0523C-'CO2EKAT', and the European Research Council under grant ERC-OPERANDOCAT (ERC-725915). BRC, AB and JR acknowledge support by Climate-KIC under the En$CO_2$re project, and AB and JR also of the Carlsberg Foundation (grant CF15-0165) and the Innovation Fund Denmark (grand solution ProActivE 5124-00003A)

## References

[1] Y. Hori, Electrochemical CO 2 Reduction on Metal Electrodes, Mod. Asp. Electrochem. (2008) 89–189. doi:10.1007/978-0-387-49489-0_3.

[2] M. Jitaru, D. a. Lowy, M. Toma, B.C. Toma, L. Oniciu, Electrochemical reduction of carbon dioxide on flat metallic cathodes, J. Appl. Electrochem. 27 (1997) 875–889. doi:10.1023/1018441316386.

[3] K.W. Frese, Electrochemical Reduction of Co2 At Solid Electrodes, in: Electrochem. Electrocatal. React. Carbon Dioxide, Elsevier B.V., 1993: pp. 145–216. doi:10.1016/B978-0-444-88316-2.50010-3.

[4] K.P. Kuhl, E.R. Cave, D.N. Abram, T.F. Jaramillo, New Insights into the Electrochemical Reduction of Carbon Dioxide on Metallic Copper Surfaces,

Energy Environ. Sci. 5 (2012) 7050–7059. doi:10.1039/c2ee21234j.

[5] E. V. Kondratenko, G. Mul, J. Baltrusaitis, G.O. Larrazábal, J. Pérez-Ramírez, Status and perspectives of CO2 conversion into fuels and chemicals by catalytic, photocatalytic and electrocatalytic processes, Energy Environ. Sci. 6 (2013) 3112. doi:10.1039/c3ee41272e.

[6] G. Centi, E.A. Quadrelli, S. Perathoner, Catalysis for CO2 conversion: a key technology for rapid introduction of renewable energy in the value chain of chemical industries, Energy Environ. Sci. 6 (2013) 1711. doi:10.1039/c3ee00056g.

[7] D.D. Zhu, J.L. Liu, S.Z. Qiao, Recent Advances in Inorganic Heterogeneous Electrocatalysts for Reduction of Carbon Dioxide, Adv. Mater. 28 (2016) 3423–3452. doi:10.1002/adma.201504766.

[8] B. Kumar, J.P. Brian, V. Atla, S. Kumari, K.A. Bertram, R.T. White, J.M. Spurgeon, New trends in the development of heterogeneous catalysts for electrochemical CO2reduction, Catal. Today. 270 (2016) 19–38. doi:10.1016/j.cattod.2016.02.006.

[9] Q. Lu, F. Jiao, Electrochemical CO2 reduction: Electrocatalyst, reaction mechanism, and process engineering, Nano Energy. 29 (2016) 439–456. doi:10.1016/j.nanoen.2016.04.009.

[10] F. Li, D.R. Macfarlane, J. Zhang, Recent Advances in Nanoengineering of Electrocatalysts for CO 2 Reduction, Nanoscale. (2018). doi:10.1039/C7NR09620H.

[11] Y. Cao, X. He, N. Wang, H.-R. Li, L.-N. He, Photochemical and Electrochemical Carbon Dioxide Utilization with Organic Compounds, Chinese J. Chem. 36 (2018) 644–659. doi:10.1002/cjoc.201700742.

[12] D.T. Whipple, P.J.A. Kenis, Prospects of CO2utilization via direct heterogeneous electrochemical reduction, J. Phys. Chem. Lett. 1 (2010) 3451–3458. doi:10.1021/jz1012627.

[13] A.J. Martín, G.O. Larrazábal, J. Pérez-Ramírez, Towards sustainable fuels and chemicals through the electrochemical reduction of CO 2 : lessons from water electrolysis, Green Chem. 17 (2015) 5114–5130. doi:10.1039/C5GC01893E.

[14] J. Qiao, Y. Liu, F. Hong, J. Zhang, A review of catalysts for the electroreduction of carbon dioxide to produce low-carbon fuels, Chem. Soc. Rev. 43 (2014) 631–675. doi:10.1039/C3CS60323G.

[15] C. Campbell, Bimetallic Surface Chemistry, Annu. Rev. Phys. Chem. 41 (1990) 775–837. doi:10.1146/annurev.physchem.41.1.775.

[16] M. Watanabe, Design of Alloy Electrocatalysts for CO2 Reduction, J. Electrochem. Soc. 138 (1991) 3382. doi:10.1149/1.2085417.

[17] Z. Chang, S. Huo, W. Zhang, J. Fang, H. Wang, The Tunable and Highly Selective Reduction Products on Ag@Cu Bimetallic Catalysts Toward CO 2 Electrochemical Reduction Reaction, J. Phys. Chem. C. 121 (2017) 11368–11379. doi:10.1021/acs.jpcc.7b01586.

[18] Y. Li, Q. Sun, Recent Advances in Breaking Scaling Relations for Effective Electrochemical Conversion of CO2, Adv. Energy Mater. 6 (2016) 1600463. doi:10.1002/aenm.201600463.

[19] A. Jedidi, S. Rasul, D. Masih, L. Cavallo, K. Takanabe, Generation of Cu–In alloy surfaces from CuInO 2 as selective catalytic sites for CO 2 electroreduction, (n.d.). doi:10.1039/c5ta05669a.

[20] Z.B. Hoffman, T.S. Gray, K.B. Moraveck, T.B. Gunnoe, G. Zangari, Electrochemical Reduction of Carbon Dioxide to Syngas and Formate at Dendritic Copper–Indium Electrocatalysts, ACS Catal. 7 (2017) 5381–5390. doi:10.1021/acscatal.7b01161.

[21] S.Y. Choi, S.K. Jeong, H.J. Kim, I.H. Baek, K.T. Park, Electrochemical Reduction of Carbon Dioxide to Formate on Tin-Lead Alloys, ACS Sustain. Chem. Eng. 4 (2016) 1311–1318. doi:10.1021/acssuschemeng.5b01336.

[22] D. Ren, B.S.H. Ang, B.S. Yeo, Tuning the Selectivity of Carbon Dioxide Electroreduction toward Ethanol on Oxide-Derived CuxZn Catalysts, ACS Catal. 6 (2016) 8239–8247. doi:10.1021/acscatal.6b02162.

[23] J. Christophe, T. Doneux, C. Buess-Herman, Electroreduction of Carbon Dioxide on Copper-Based Electrodes: Activity of Copper Single Crystals and Copper-Gold Alloys, Electrocatalysis. 3 (2012) 139–146. doi:10.1007/s12678-012-0095-0.

[24] J.P. Grote, A.R. Zeradjanin, S. Cherevko, A. Savan, B. Breitbach, A. Ludwig, K.J.J. Mayrhofer, Screening of material libraries for electrochemical CO2reduction catalysts – Improving selectivity of Cu by mixing with Co, J. Catal. 343 (2016) 248–256. doi:10.1016/j.jcat.2016.02.026.

[25] S. Lee, G. Park, J. Lee, Importance of Ag-Cu Biphasic Boundaries for Selective Electrochemical Reduction of CO2to Ethanol, ACS Catal. 7 (2017) 8594–8604. doi:10.1021/acscatal.7b02822.

[26] D. Kim, J. Resasco, Y. Yu, A.M. Asiri, P. Yang, Synergistic geometric and electronic effects for electrochemical reduction of carbon dioxide using gold-copper bimetallic nanoparticles, Nat. Commun. 5 (2014) 1–8. doi:10.1038/ncomms5948.

[27] P. Hirunsit, W. Soodsawang, J. Limtrakul, CO2 electrochemical reduction to methane and methanol on copper-based alloys: Theoretical insight, J. Phys. Chem. C. 119 (2015) 8238–8249. doi:10.1021/acs.jpcc.5b01574.

[28] A.S. Varela, C. Schlaup, Z.P. Jovanov, P. Malacrida, S. Horch, I.E.L. Stephens, I. Chorkendorff, CO2 electroreduction on well-defined bimetallic surfaces: Cu overlayers on Pt(111) and Pt(211), J. Phys. Chem. C. 117 (2013) 20500–20508. doi:10.1021/jp406913f.

[29] S. Rasul, D.H. Anjum, A. Jedidi, Y. Minenkov, L. Cavallo, K. Takanabe, SI-A Highly Selective Copper – Indium Bimetallic Electrocatalyst for the Electrochemical Reduction of Aqueous CO 2 to CO, Angew. Chemie - Int. Ed. (2015) 1–6. doi:10.1002/anie.201410233.

[30] T.A. Maark, B.R.K. Nanda, Enhancing CO 2 Electroreduction by Tailoring Strain and Ligand, (2017). doi:10.1021/acs.jpcc.7b00940.

[31] R. Reske, M. Duca, M. Oezaslan, K.J.P. Schouten, M.T.M. Koper, P.S.R.R.M.D.M.O.K.J.P.S. M. T. M. Koper, Controlling catalytic selectivities during CO 2 electro reduction on strained metal overlayers, J. Phys. Chem. Lett. (2013) 1–11.

[32] S. Sarfraz, A.T. Garcia-Esparza, A. Jedidi, L. Cavallo, K. Takanabe, Cu–Sn Bimetallic Catalyst for Selective Aqueous Electroreduction of CO $_2$ to CO, ACS

Catal. 6 (2016) 2842–2851. doi:10.1021/acscatal.6b00269.

[33] J. He, N.J. Johnson, A. Huang, C. Berlinguette, Electrocatalytic Alloys for CO2 Reduction, ChemSusChem. 11 (2017) 48–57. doi:10.1002/cssc.201701825.

[34] G.C. Bond, The origins of particle size effects in heterogeneous catalysis, Surf. Sci. 156 (1985) 966–981. doi:10.1016/0039-6028(85)90273-0.

[35] W. Tang, A.A. Peterson, A.S. Varela, Z.P. Jovanov, L. Bech, W.J. Durand, S. Dahl, J.K. Nørskov, I. Chorkendorff, The importance of surface morphology in controlling the selectivity of polycrystalline copper for CO2 electroreduction, Phys. Chem. Chem. Phys. 14 (2012) 76–81. doi:10.1039/C1CP22700A.

[36] A.P. O’Mullane, From single crystal surfaces to single atoms: investigating active sites in electrocatalysis, Nanoscale. 6 (2014) 4012–4026. doi:10.1039/C4NR00419A.

[37] J. Solla-Gullón, F.J. Vidal-Iglesias, J.M. Feliu, Shape dependent electrocatalysis, Annu. Reports Sect. “C” (Physical Chem. 107 (2011) 263. doi:10.1039/c1pc90010b.

[38] A. Dutta, M. Rahaman, N.C. Luedi, M. Mohos, P. Broekmann, Morphology Matters: Tuning the Product Distribution of CO2Electroreduction on Oxide-Derived Cu Foam Catalysts, ACS Catal. 6 (2016) 3804–3814. doi:10.1021/acscatal.6b00770.

[39] C. Reller, R. Krause, E. Volkova, B. Schmid, S. Neubauer, A. Rucki, M. Schuster, G. Schmid, Selective Electroreduction of CO 2 toward Ethylene on Nano Dendritic Copper Catalysts at High Current Density, Adv. Energy Mater. 7 (2017) 1602114. doi:10.1002/aenm.201602114.

[40] R. Reske, H. Mistry, F. Behafarid, B.R. Cuenya, P. Strasser, Particle Size Effects in the Catalytic Electroreduction of CO2 on Cu Nanoparticles, J Amer Chem Soc. 136 (2014) 6978–6986. doi:10.1021/ja500328k |.

[41] H. Mistry, R. Reske, Z. Zeng, Z. Zhao, J. Greeley, P. Strasser, B.R. Cuenya, Exceptional Size-Dependent Activity Enhancement in the Electroreduction of CO 2 over Au Nanoparticles, J. Am. Chem. Soc. 136 (2014) 16473–16476. doi:10.1021/ja508879j.

[42] H. Liao, A. Fisher, Z.J. Xu, Surface Segregation in Bimetallic Nanoparticles: A Critical Issue in Electrocatalyst Engineering, Small. 11 (2015) 3221–3246. doi:10.1002/smll.201403380.

[43] H. Mistry, A.S. Varela, S. Kühl, P. Strasser, B.R. Cuenya, Nanostructured electrocatalysts with tunable activity and selectivity, Nat. Rev. Mater. 1 (2016) 16009. doi:10.1038/natrevmats.2016.9.

[44] K.J.J. Mayrhofer, V. Juhart, K. Hartl, M. Hanzlik, M. Arenz, Adsorbate-Induced surface Segregation for core-shell nanocatalysts, Angew. Chemie - Int. Ed. 48 (2009) 3529–3531. doi:10.1002/anie.200806209.

[45] E. Bertheussen, T. V Hogg, Y. Abghoui, A.K. Engstfeld, I. Chorkendorff, I.E.L. Stephens, Electroreduction of CO on Polycrystalline Copper at Low Overpotentials, ACS Energy Lett. 3 (2018) 634–640. doi:10.1021/acsenergylett.8b00092.

[46] G. Kästle, H.G. Boyen, F. Weigl, G. Lengl, T. Herzog, P. Ziemann, S. Riethmüller, O. Mayer, C. Hartmann, J.P. Spatz, M. Möller, M. Ozawa, F. Banhart, M.G. Garnier, P. Oelhafen, Micellar Nanoreactors - Preparation and Characterization of Hexagonally Ordered Arrays of Metallic Nanodots, Adv. Funct. Mater. 13 (2003) 853–861. doi:10.1002/adfm.200304332.

[47] J. Eastoe, M.J. Hollamby, L. Hudson, Recent advances in nanoparticle synthesis with reversed micelles, Adv. Colloid Interface Sci. 128–130 (2006) 5–15. doi:10.1016/j.cis.2006.11.009.

[48] A. Bagger, W. Ju, A.S. Varela, P. Strasser, J. Rossmeisl, Electrochemical $CO_2$ Reduction: A Classification Problem, ChemPhysChem. 18 (2017) 3266–3273. doi:10.1002/cphc.201700736.

[49] A. Ankudinov, B. Ravel, Real-space multiple-scattering calculation and interpretation of x-ray-absorption near-edge structure, Phys. Rev. B - Condens. Matter Mater. Phys. 58 (1998) 7565–7576. doi:10.1103/PhysRevB.58.7565.

[50] J.J. Rehr, Theoretical approaches to x-ray absorption fine structure, Rev. Mod. Phys. 72 (2000) 621–654. doi:10.1103/RevModPhys.72.621.

[51] A. Larsen, J. Mortensen, J. Blomqvist, I. Castelli, R. Christensen, M. Dulak, J.

Friis, M. Groves, B. Hammer, C. Hargus, Others, The Atomic Simulation Environment—A Python library for working with atoms, J. Phys. Condens. Matter. 2 (2017).

[52] B. Hammer, L.B. Hansen, J.K. Nørskov, Improved adsorption energetics within density-functional theory using revised Perdew-Burke-Ernzerhof functionals, Phys. Rev. B - Condens. Matter Mater. Phys. 59 (1999) 7413–7421. doi:10.1103/PhysRevB.59.7413.

[53] J. Enkovaara, C. Rostgaard, J.J. Mortensen, J. Chen, M. Dułak, L. Ferrighi, J. Gavnholt, C. Glinsvad, V. Haikola, H.A. Hansen, H.H. Kristoffersen, M. Kuisma, A.H. Larsen, L. Lehtovaara, M. Ljungberg, O. Lopez-Acevedo, P.G. Moses, J. Ojanen, T. Olsen, V. Petzold, N.A. Romero, J. Stausholm-Møller, M. Strange, G.A. Tritsaris, M. Vanin, M. Walter, B. Hammer, H. Häkkinen, G.K.H. Madsen, R.M. Nieminen, J.K. Nørskov, M. Puska, T.T. Rantala, J. Schiøtz, K.S. Thygesen, K.W. Jacobsen, Electronic structure calculations with GPAW: A real-space implementation of the projector augmented-wave method, J. Phys. Condens. Matter. 22 (2010) 253202. doi:10.1088/0953-8984/22/25/253202.

[54] J. Wellendorff, K.T. Lundgaard, A. Møgelhøj, V. Petzold, D.D. Landis, J.K. Nørskov, T. Bligaard, K.W. Jacobsen, Density functionals for surface science: Exchange-correlation model development with Bayesian error estimation, Phys. Rev. B - Condens. Matter Mater. Phys. 85 (2012) 32–34. doi:10.1103/PhysRevB.85.235149.

[55] M.C. Biesinger, L.W.M. Lau, A.R. Gerson, R.S.C. Smart, Resolving surface chemical states in XPS analysis of first row transition metals, oxides and hydroxides: Sc, Ti, V, Cu and Zn, Appl. Surf. Sci. 257 (2010) 887–898. doi:10.1016/j.apsusc.2010.07.086.

[56] M.C. Biesinger, B.P. Payne, A.P. Grosvenor, L.W.M. Lau, A.R. Gerson, R.S.C. Smart, Resolving surface chemical states in XPS analysis of first row transition metals, oxides and hydroxides: Cr, Mn, Fe, Co and Ni, Appl. Surf. Sci. 257 (2011) 2717–2730. doi:10.1016/j.apsusc.2010.10.051.

[57] C. Shi, H.A. Hansen, A.C. Lausche, J.K. Nørskov, Trends in electrochemical CO2 reduction activity for open and close-packed metal surfaces, Phys. Chem. Chem.

Phys. 16 (2014) 4720. doi:10.1039/c3cp54822h.

[58] A.A. Peterson, F. Abild-Pedersen, F. Studt, J. Rossmeisl, J.K. Nørskov, How copper catalyzes the electroreduction of carbon dioxide into hydrocarbon fuels, Energy Environ. Sci. 3 (2010) 1311. doi:10.1039/c0ee00071j.

[59] C.J. Powell, A. Jablonski, NIST Electron Inelastic-Mean-Free-Path Database 71, Version 1.1, Nat'l Std. Ref. Data Ser. (NIST NSRDS) -. (2000). https://www.nist.gov/publications/nist-electron-inelastic-mean-free-path-database-71-version-11?pub_id=906024 (accessed June 19, 2018).

[60] R.W.G.Wyckoff, Crystal Structures Volume 1, Second edi, New York: Interscience Publishers, New York, NY, 1963.

[61] P.M. Diehm, P. Ágoston, K. Albe, Size-dependent lattice expansion in nanoparticles: Reality or anomaly?, ChemPhysChem. 13 (2012) 2443–2454. doi:10.1002/cphc.201200257.

[62] J.S. Vermaak, C.W. Mays, D. Kuhlmann-Wilsdorf, On surface stress and surface tension, Surf. Sci. 12 (1968) 128–133. doi:10.1016/0039-6028(68)90118-0.

[63] H.J. Wasserman, J.S. Vermaak, on the Determination of the Surface Stress of Copper and Platinum, Surf. Sci. 32 (1972) 168–174.

[64] E.A. Mcneill, F.R. Scholer, Molecular Structure of the Gaseous Metal Carbonyl Hydrides of Manganese, Iron, and Cobalt, (n.d.). https://pubs.acs.org/doi/pdf/10.1021/ja00461a011 (accessed July 2, 2018).

[65] A. V. Ruban, H.L. Skriver, J.K. Nørskov, Surface segregation energies in transition-metal alloys, Phys. Rev. B - Condens. Matter Mater. Phys. 59 (1999) 15990–16000. doi:10.1103/PhysRevB.59.15990.

[66] A. Bagger, W. Ju, A.S. Varela, P. Strasser, J. Rossmeisl, Single site porphyrine-like structures advantages over metals for selective electrochemical CO2 reduction, Catal. Today. 288 (2017) 74–78. doi:10.1016/J.CATTOD.2017.02.028.

[67] H. Mistry, F. Behafarid, R. Reske, A.S. Varela, P. Strasser, B. Roldan Cuenya, Tuning Catalytic Selectivity at the Mesoscale via Interparticle Interactions, ACS Catal. 6 (2016) 1075–1080. doi:10.1021/acscatal.5b02202.

**Miguel Bernal** studied Chemistry and received a B.S. in chemistry (2008-2013) and a M.S. in chemical sciences (2013-2015) at the National Autonomous University of Mexico. He is carrying out his doctoral studies at Ruhr-University Bochum (Germany) and is part of the International Max Planck Research School for Interface Controlled Materials for Energy Conversion (IMPRS-Surmat). His scientific interests involve environmental chemistry, clean energy conversion, electrochemistry, nano materials and catalysis. His current research is focused on the development, characterization and evaluation of nano catalysts for the electrochemical reduction of carbon dioxide.

**Alexander Bagger** studied Applied Physics (2010-2016) at the Technical University of Denmark (DTU) where he obtained a B.S. and a M. S. He is currently completing his Ph.D. in the group of Professor Jan Rossmeisl at the Department of Chemistry at the University of Copenhagen (Denmark). His research is focused on understanding electrocatalytic reactions from atomic level based on Density Functional Theory calculations. A special emphasis is in understanding the electrocatalytic reduction of CO2/CO and in electrolyte effects in the electrochemical interface region.

**Fabian Scholten** studied Physics (2010-2016) at the Ruhr-University Bochum where he obtained a B.Sc. and a MSc. He currently in his second Ph.D. year in the group of Prof. Dr. Roldan. His research is focused on the electrocatalytic reduction of $CO_2$ with special emphasis to the role of the chemical state and structure of copper based catalysts.

**Ilya Sinev** holds Ph.D. (2009) in catalysis from Zelinsky Institute of Organic Chemistry (Moscow, Rusia), and an M.S. (2004) in physics from Lomonosov Moscow State University. He works in Ruhr-University Bochum (Germany) as a postdoctoral scholar and has several years work experience in the area of heterogeneous (electro) catalysis. Ilya Sinev research interests include studying structure-activity relationships in solid-state catalysts using surface science and synchrotron methods. He has published more than 40 peer-reviewed manuscripts in the major journals in the areas of physical chemistry, electro- and heterogeneous catalysis.

**Arno Bergmann** is PostDoc in the Department of Interface Science of the Fritz-Haber-received his PhD degree in the Electrochemical Energy, Catalysis and Materials Science Laboratory of Technische Universität Berlin in 2016. Prior to joining the Fritz-Haber-Institute, he was PostDoc at the Helmholtz Zentrum Berlin für Materialien und Energie. His research focuses on model electrocatalysts based on transition metal oxides and X-ray-based operando diffraction and absorption studies.

**Mahdi Ahmadi** got his B.S. in physics (2005–2009) at Sharif university of technology, master in atomic and molecular physics at the university of Tehran and carried out his Ph.D. (2011–2016) at the university of central Florida. He is currently a postdoctoral research associate at Cornell university in the group of Professor Héctor D. Abruña. His current research interests include electrocatalytic processes as well as the synthesis, characterization, and electrocatalytic properties of metal alloys and oxides nanoparticles with application in fuel cells.

**Jan Rossmeisl** he obtained a M. S. on Applied Physics (2000) and a Ph.D. (2004) from the Technical University of Denmark (DTU). At DTU he became an Assistant Professor (2006-2009) and then an Associate Professor (2009-2015). Currently he is Professor at the Department of Chemistry at the University of Copenhagen (Danemark). His research interests are: Density functional theory, Theoretical Electro-chemistry, Solid liquid interface, Catalysis, Fuel cells and Fuel generation, Design of alloys and oxides for electrodes. His specialties are: Computer modeling at the atomic level, Quantum mechanics, Thermo chemistry, Physical chemistry.

**Beatriz Roldán Cuenya** received a B.S. in Physics from the University of Oviedo (Spain, 1998) and a Ph.D. in Physics from the University of Duisburg-Essen (Germany, 2001). She did a postdoc in Chemical Engineering at the University of California Santa Barbara (2001–2003). She was a Professor of Physics at the University of Central Florida (USA, 2004-2012) and at the Ruhr-University Bochum (Germany, 2013-2017). Currently, she is the director of the Department of Interface Science at the Fritz-Haber Institute of the Max Planck Society (Berlin, Germany). She studies catalytic processes at the nanoscale based on *operando* microscopic and spectroscopic characterization.